Elucidating the Transition of 3D Morphological Evolution of Binary Alloys in Molten Salts with Metal Ion Additives

Xiaoyang Liu, Kaustubh K. Bawane, Charles Clark, Yuxiang Peng, Michael E. Woods, Phillip Halstenberg, Xianghui Xiao, Wah-Keat Lee, Lu Ma, Steven Ehrlich, Sheng Dai, Katsuyo Thornton, Mingyuan Ge, Ruchi Gakhar, Lingfeng He, and Yu-chen Karen Chen-Wiegart*

Cite This: https://doi.org/10.1021/acsami.4c02049

Read Online

ACCESS | Metrics & More | Article Recommendations | SI Supporting Information

ABSTRACT: Molten salts serve as effective high-temperature heat transfer fluids and thermal storage media used in a wide range of energy generation and storage facilities, including concentrated solar power plants, molten salt reactors and high-temperature batteries. However, at the salt–metal interfaces, a complex interplay of charge-transfer reactions involving various metal ions, generated either as fission products or through corrosion of structural materials, takes place. Simultaneously, there is a mass transport of ions or atoms within the molten salt and the parent alloys. The precise physical and chemical mechanisms leading to the diverse morphological changes in these materials remain unclear. To address this knowledge gap, this work employed a combination of synchrotron X-ray nanotomography and electron microscopy to study the morphological and chemical evolution of Ni-20Cr in molten $KCl\text{-}MgCl_2$, while considering the influence of metal ions (Ni^{2+}, Ce^{3+}, and Eu^{3+}) and variations in salt composition. Our research suggests that the interplay between interfacial diffusivity and reactivity determines the morphological evolution. The summary of the associated mass transport and reaction processes presented in this work is a step forward toward achieving a fundamental comprehension of the interactions between molten salts and alloys. Overall, the findings offer valuable insights for predicting the diverse chemical and structural alterations experienced by alloys in molten salt environments, thus aiding in the development of protective strategies for future applications involving molten salts.

KEYWORDS: high-temperature corrosion, dealloying, TXM, STEM, materials kinetics
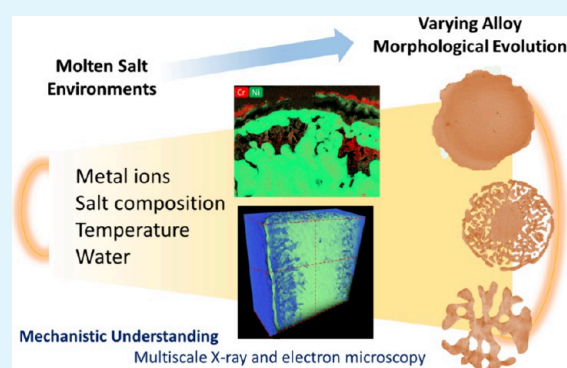
INTRODUCTION

There is a resurgence in the use of molten salts as coolants or reaction media for large-scale energy facilities, including molten salt reactors,[1] concentrating solar power plants[2] and electrolytes for molten salt batteries.[3] However, structural alloys undergo various morphological changes in molten salts, leading to degradation.[4,5] A prior study aggregated and graphed historical molten fluoride and chloride salt corrosion data with experimental characteristics, including salt purification, temperature, and experimental setups used from 1960 to 2016.[4] Many previous studies have been focused on the relationship between the processing conditions and morphological and chemical changes in engineering alloys. However, there remains a critical need to understand fundamentally how the complex chemical and physical processes and their interplay at solid–liquid interfaces cause structural evolution to different morphologies. Such fundamental processes are further affected by molten salt environmental factors, such as temperature,[6] irradiation,[7] and impurities, including O_2, H_2O, hydroxides, fission products, and corrosion products from structural materials.[8] Thus, understanding the interfacial reactions, diffusion and their relation-

ships with the morphological changes is critical in developing a strong scientific basis for applying molten salts in energy technologies.

In molten salt reactors, metal ions accumulate in the molten salt as fission products and through corrosion of structural materials. These metal ions can change the salt properties and induce reactivity with the structural alloys. It is critical to understand how the alloys react with the salt in the presence of different metal ions. Metal ions formed by the corrosion of structural materials, such as Ni^{2+}, Fe^{3+}, and Fe^{2+}, can cause the molten salt to be more oxidizing, which promotes the corrosion of Cr.[9] Among fission products, rare earth elements such as Ce, Eu, La, Sm, and Pr can enter the molten salt as stable ions and

then act as oxidants in the system.[10,11] Previous studies have analyzed the local structures of metallic ions in molten salts[12] and determined the diffusion coefficients with electrochemical techniques[13] to understand their influence on mass transport. Thermodynamic analysis has also been instrumental in providing temperature-dependent redox potentials to determine whether metal ions or fission products have the tendency to drive corrosion reactions in molten salts.[11] Experimentally, the level of corrosion is commonly evaluated by mass loss or corrosion depth, such as by mapping out the depths of Cr depletion zones in Ni-based alloys.[11,14] However, further studies are required to understand how the underlying kinetics and mechanisms, including those for chemical reactions and diffusion at the metal−salt interfaces, are impacted by the presence of these reactive ions and whether they lead to changes in morphological evolution and the corresponding corrosion rates.

This work is focused on studying the effects of various additives ($NiCl_2$, $CeCl_3$, and $EuCl_3$) on the morphological evolution of model binary alloys in molten salt. By combining synchrotron X-ray nanotomography for 3D imaging with 2D X-ray absorption near edge spectroscopy (XANES) imaging and scanning transmission electron microscopy (STEM), a multi-modal imaging approach enables studies of the morphological and chemical changes of Ni-20Cr in molten KCl-$MgCl_2$ at multiple scales. A model that considers competition between the interfacial reaction and diffusion was proposed to offer a potential cause of the observed variation in the morphology and chemical distributions. Direct visualization of morphological evolution enables the determination of how fundamental characteristics such as the chemical reactivities and diffusivities of salts and alloys contribute to corrosion mechanisms. This study constitutes a step forward in understanding how the complex environment and fundamental parameters drive molten salt−material interactions and how different physical and chemical processes interact and lead to different 3D morphologies of alloys.

■ EXPERIMENTAL SECTION

Sample Preparation. Purification of $MgCl_2$ followed a procedure established in previous studies by the team.[15] The purified $MgCl_2$ salt was mixed with KCl (purchased from Sigma-Aldrich as 99.999% Suprapur reagent grade) in an Ar-filled glovebox in the required proportion to form a eutectic mixture. $NiCl_2$ (1 wt %, 99.99%, Aldrich Chem. Co.) was then mixed with the eutectic KCl-$MgCl_2$. The mixed salt was melted in a quartz crucible using a custom heater inside the glovebox at ∼650 °C for ∼3 h. The mixtures of KCl-$MgCl_2$ with $CeCl_3$ and $EuCl_3$ were prepared inside an Ar-filled glovebox at Idaho National Laboratory (INL). KCl-$MgCl_2$ 50:50 molar ratio was prepared by mixing and melting KCl and $MgCl_2$ in a glassy carbon crucible (GAZ 5, HTW Germany) at 600 °C for 6 h. The glassy carbon crucible was cleaned with isopropanol and baked under vacuum at 120 °C overnight, followed by baking inside the Ar-filled glovebox at 700 °C for 4 h to remove any absorbed moisture or adsorbed organic matter. Upon cooling, the mixture was crushed with an agate mortar and pestle and loaded with 1 wt % $CeCl_3$ or $EuCl_3$ in separate glassy carbon crucibles. The mixed compositions were then heated at 550 °C for 2 h and crushed to fine powders upon cooling.

Ni-20Cr microwire samples encapsulated with salts and additives in a double-capillary design were prepared by following an established method.[16,17] The protocol is described briefly below: quartz capillaries with 0.1 and 1.0 mm outer diameters (OD, Charles Supper) were baked at 500 °C to remove potential organic contaminants and then together with Ni-20Cr microwires (99.5% pure, as-drawn, 20 μm diameter, Goodfellow, USA-NI055105) in an oven (∼120 °C) for at least 3 h to remove surface moisture. In an Ar-filled glovebox, the Ni-20Cr wire was placed in the 0.1 mm capillary, and molten salt with additives was extracted into the capillary. The quartz capillary with the microwire and the solidified salt was placed into a larger capillary and sealed temporarily with epoxy. After the epoxy was cured, the sample was removed from the glovebox and immediately flame-sealed using a benchtop hydrogen torch (Rio Grande).

Synchrotron X-ray Nanotomography and TEM Measurements. These ex situ experiments were conducted on the samples with $NiCl_2$ and $CeCl_3$ additives. The assembled samples were first studied with X-ray nanotomography and spectroscopic imaging at the Full Field X-ray Imaging (FXI) beamline (18-ID) at NSLS-II of Brookhaven National Laboratory.[18] A box furnace was preheated to 700 °C. The samples were then moved into the box furnace and heated for the designated time to observe 3D morphological evolution of the same sample. Evolution of the sample at 700 °C in molten KCl-$MgCl_2$ containing $EuCl_3$ and anhydrous $NiCl_2$ was studied in situ with a miniature furnace[19] integrated with transmission X-ray microscopy (TXM) at FXI. The X-ray incident energy used was 8.333 keV to optimize image contrast. Images were captured using a lens-coupled CCD detector with 2560 × 2560 pixels, magnification at 325 and camera binning of 2 × 2. The effective pixel size was 40 nm. The magnification for the in situ experiment of the sample with anhydrous $NiCl_2$ was 302.4, with an effective pixel size of 43.2 nm. Over 800 projections were collected per tomography with an exposure time of ∼50 ms per projection image. Tomographic reconstruction was conducted using the python package Tomopy.[20] 2D XANES images of the sample were obtained by scanning the Ni K-edge from 8.251 to 8.613 keV. PyXAS[21] and Athena[22] software were used to process the spectroscopic imaging data. In addition, standard XANES spectra across the Ni K-edge were also measured: a standard Ni foil was measured at the FXI beamline; pristine $NiCl_2$ (purchased from Aldrich Chem. Co.) as used in the samples, as well as anhydrous $NiCl_2$ powder (99.99%, purchased from Sigma-Aldrich) and NiO powder (Sigma-Aldrich) were measured at the Quick X-ray Absorption and Scattering (QAS) beamline of NSLS-II. The $NiCl_2$ standards were mixed with boron nitride (BN) powder and loaded into a 1.5 mm (OD) quartz capillary in the glovebox. The capillary was removed from the glovebox with a Swagelok Fitting, evacuated with a rough vacuum pump for 5 min, and then flame-sealed immediately. The NiO standard was prepared on Kapton tape.

Commercial data visualization and analysis software Avizo (Thermo Fisher Scientific, v. 9.3.0) was used to create 2D pseudo cross-sectional views and 3D volume rendering views. For the in situ tomography data sets, image cross-correlation was used to align the whole tomography time series via volume registration from fast Fourier transforms of the 3D volumes using a custom Python program.[21] Thresholding segmentation was performed to differentiate Ni-20Cr and pores. The volume change and porosity were then quantified; the detailed segmentation and quantification method can be found in the Supporting Information and Figure S1.

After the synchrotron X-ray measurements, the outer quartz capillaries of the samples (with $CeCl_3$ and $NiCl_2$) were broken manually inside an Ar-filled glovebox to recover the inner quartz capillaries containing corroded Ni-20Cr microwires. Each inner quartz capillary was loaded on a scanning electron microscopy (SEM) stub with a carbon tape and shipped to INL for TEM sample preparation and analysis. The sample was then placed inside a shielded Thermo Scientific plasma focused ion beam (PFIB) dual beam system with a sample loading port attached to an Ar-filled glovebox. The samples were not exposed to air during shipment and transfer. The inner quartz capillary sample was coated with gold using a sputter coater to avoid charging during PFIB sample preparation. An Xe ion beam in PFIB was used to cut a small region of the glass capsule to expose the corroded Ni-20Cr microwire inside. A piece of corroded Ni-20Cr microwire was cut using the Xe ion beam and lifted out using EasyLift EX Nano-Manipulator. The lifted-out piece was then placed on an empty SEM stub with a carbon tape and welded using platinum. The sample was then transferred to a shielded Thermo Scientific Quanta 3D focused ion beam (FIB) with a loading port attached to an Ar-filled glovebox. TEM
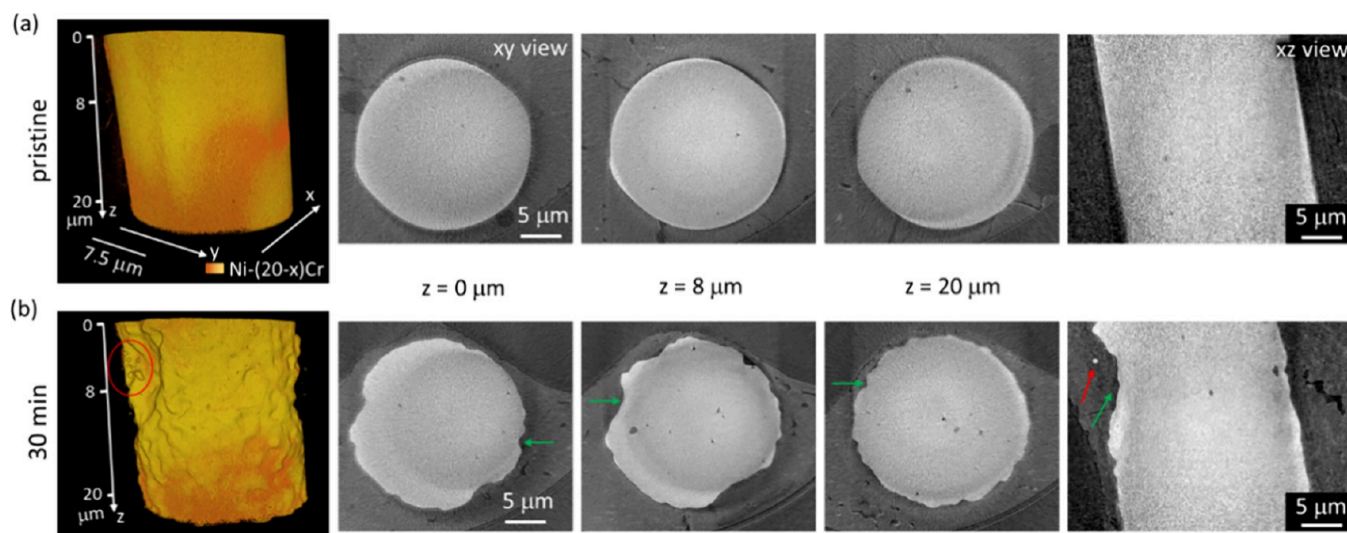
Figure 1. 3D and pseudo-2D *xy* views at different *z* locations (0, 8, and 20 μm) and a pseudo *xz* view of pristine Ni-20Cr (the top row) and Ni-(20-*x*)Cr (the bottom row) after reacting with 1 wt % CeCl$_3$ in molten KCl-MgCl$_2$ (50−50 mol %) for 30 min: (a) pristine Ni-20Cr, which was homogeneous without large pores or holes; (b) Ni-(20-*x*)Cr after molten salt corrosion for 30 min at 700 °C, which showed surface voids. The green arrows indicate the holes on the surface. The red circle and arrow indicate the particles observed in the remnant salt.

lamellae samples along the transverse direction of the Ni-20Cr microwire were prepared using the lift-out technique inside FIB. TEM lamellae were mounted on a Cu TEM half-grid and then placed into an airtight container for transfer. The corroded Ni-20Cr microwires had a thin remaining salt layer after corrosion which allowed studying the alloy−salt interface using TEM.

The airtight container with TEM lamellae was opened inside a glovebag (Erlab portable glovebag) with Ar atmosphere. TEM lamellae were loaded into the Gatan vacuum transfer TEM sample holder. TEM analysis was performed using a Thermo Scientific Titan Themis 200 TEM equipped with the Super-X energy dispersive X-ray spectroscopy (EDS) and the Gatan Continuum electron energy loss spectroscopy (EELS) systems. The elemental distribution in the microstructure was studied using the EDS technique and the oxidation states of dissolved alloying elements were analyzed using the EELS technique. EDS quantification was performed using the Brown-Powell ionization cross-section model using Thermo Scientific Velox software. A custom script was written in Python (JupyterLab) using HyperSpy multidimensional data analysis toolbox to measure L_3/L_2 integrated intensity ratios in EELS spectra. Oxidation state analysis was performed by comparing L_3/L_2 integrated intensity ratios of samples and that of the references. This approach was used to measure the oxidation states of transition metals in molten salts by the team.[23]

RESULTS AND DISCUSSION

Ni-20Cr Corrosion in Molten KCl-MgCl$_2$ (50−50 mol %) with 1 wt % CeCl$_3$. The 3D and 2D (*xy* and *xz* views) morphologies of pristine Ni-20Cr and Ni-(20-*x*)Cr reacted with 1 wt % CeCl$_3$ in molten KCl-MgCl$_2$ (50−50 mol %) are shown in Figure 1 (Video S1). For pristine Ni-20Cr (Figure 1a), the 3D and pseudo2D *xy* views at different locations (0, 8, and 20 μm) in the *z* direction shows a smooth surface without pores. However, Figure 1b shows that after 30 min of reaction at 700 °C, the sample was corroded with loss of material on the surface. Some particles were observed, highlighted with a red circle in the 3D view and a red arrow in the 2D *xz* view. While surface voids or dimple-like features were observed in the 30 min sample (green arrows), no pores or cracks were observed. Previous experiments, in which Ni-20Cr samples were exposed to molten KCl-MgCl$_2$ without the addition of CeCl$_3$ showed morphologies

having intergranular corrosion at 500 °C,[17] and bicontinuous pores at 800 °C[16]; those features are not observed here.

After synchrotron X-ray nanotomography, the same sample was characterized by STEM/EDS without air or moisture exposure to study the elemental distributions and chemical states of the corrosion products. Figure 2 shows the STEM high-angle annular dark-field (HAADF) image and the elemental maps of the alloy elements (Ni and Cr) and salt elements (K, Mg, Cl). Both Ni and Cr were present in the corroded Ni-(20-*x*)Cr. Interestingly, two distinct regions were identified near the surface, and the dashed lines in Figure 2a indicate the division: the region of interest (ROI1) is the region from the surface to the grain boundaries, and ROI2 is the region extending from the grain boundaries to the center of the sample, as marked by the dashed lines. A total of 10 positions (each of which is 123.4 nm × 123.4 nm, Figure S2) were selected randomly in each ROI to quantify the Cr to Ni weight ratios, as shown in Figure 2b. The dashed red line shows the Cr to Ni weight ratio of 0.25 for pristine Ni-20Cr. For ROI1, the average Cr to Ni weight ratio was 0.09 with a standard deviation (std) of 0.03, which indicated 91.7 wt % Ni and 8.3 wt % Cr. This suggests that dealloying of Cr from the sample occurred in the surface region (within 1−2 grains below the surface) from reaction with 1 wt % CeCl$_3$ in molten KCl-MgCl$_2$ for 30 min. On the other hand, for ROI2, the average Cr to Ni weight ratio was 0.18 with a std of 0.02, which was lower than that of the pristine Cr−Ni ratio, 0.25; the composition was 84.7 wt % Ni and 15.3 wt % Cr, indicating that selective removal of Cr had already occurred in this region, which was beneath the surface region. Since no intergranular corrosion or percolation dealloying was observed, the Cr depletion in ROI2 may have occurred through bulk diffusion in the metal following a chemical reaction occurring at the metal−salt interface due to the concentration gradient between the surface and the interior of the sample. Additionally, no intergranular or intragranular pores were observed in the HAADF image, which was consistent with the observation from synchrotron X-ray nanotomography.

To further understand the corrosion process, the remnant salt was analyzed. The remnant salt region was identified from the
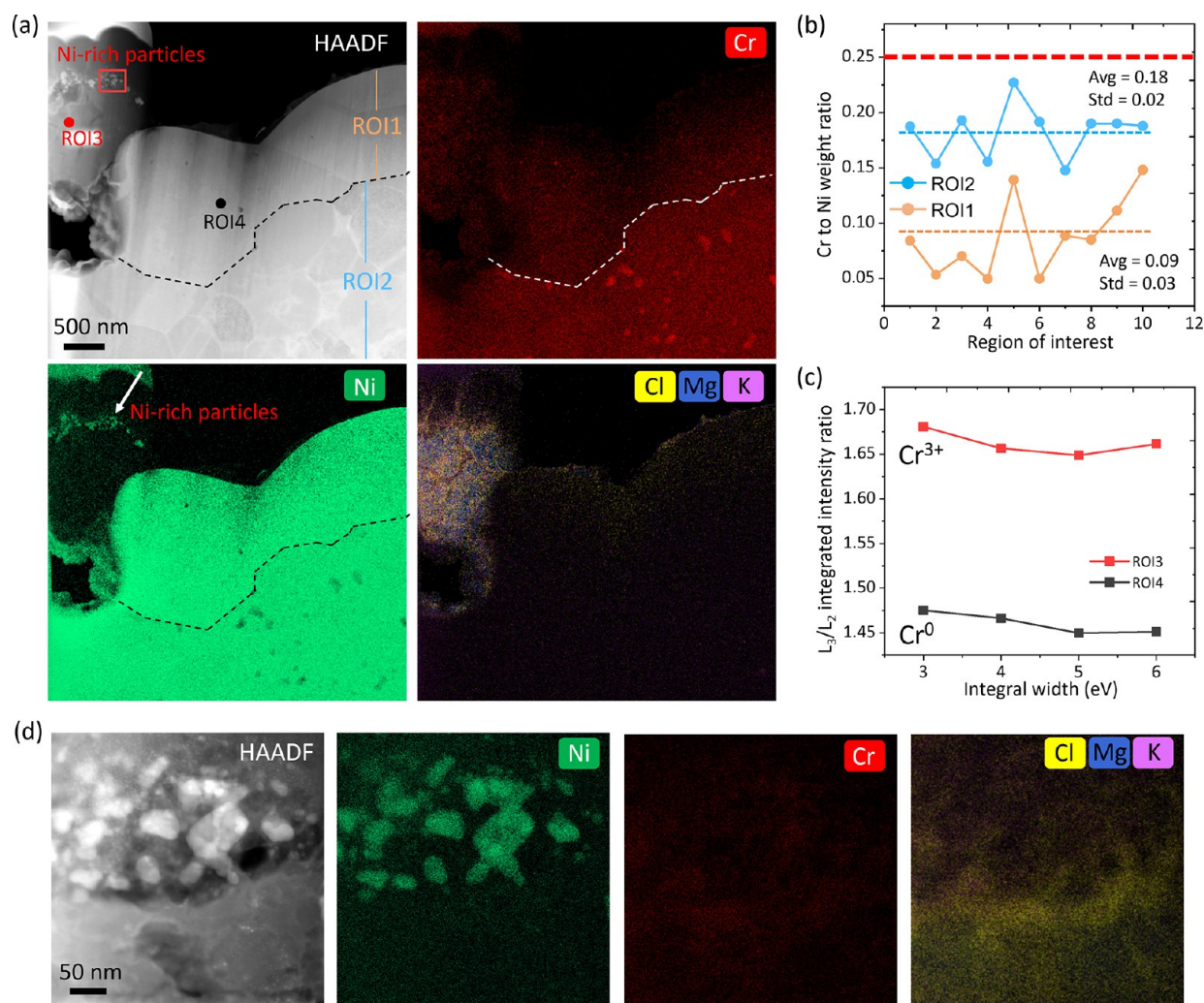
Figure 2. STEM/EDS and EELS analysis of the corroded Ni-(20-x)Cr reacting with 1 wt % $CeCl_3$ in molten KCl-$MgCl_2$ (50−50 mol %) at 700 °C for 30 min; this shows the morphologies and elemental distributions of the sample and the remnant salt. The corroded wire was not completely surrounded by the salt. (a) High-angle annular dark-field (HAADF) image from STEM and the elemental maps for Ni and Cr (alloy) and K, Mg, and Cl (salt). The dashed line is along the grain boundary. (b) Cr to Ni weight ratios in ROI1 and ROI2 in (a). (c) The Cr L_3/L_2 peak intensity ratio changed as a function of integral width in ROI3 and ROI4 in (a). (d) An expanded view shows the Ni-rich particles in the remnant salt from the region in (a) indicated with a red rectangle.

image contrast in the HAADF image and the K, Mg and Cl elemental maps. In the remnant salt, there was 6.7 at % Cr, which was higher than the Ni content at 1.6 at %. The redox potentials of $CrCl_2$/Cr and $CrCl_3$/Cr are more negative than that of $NiCl_2$/Ni[11]; thus, preferential oxidation (dissolution) of Cr occurred. The chemical states of Cr in the remnant salt and Ni-(20-x)Cr (ROI3 and ROI4 in Figure 1a) were analyzed by EELS. The Cr L_3/L_2 integrated intensity ratio was ~1.6 for the integral widths of 3, 4, 5, and 6 eV (Table S1) at ROI3, which was similar to the reference $CrCl_3$,[23] suggesting the presence of Cr^{3+}. For ROI4, the Cr L_3/L_2 integrated intensity ratio was ~1.4, which was similar to the reference of Cr^0, suggesting that Cr was not oxidized in the alloy. Note that some Ni-rich particles were observed in the Ni elemental map and the HAADF image for the remnant salt region, as indicated by a white arrow in Figure 2a. Figure 2d shows a magnified view of these Ni-rich nanoparticles. Their sizes were smaller than the particles observed with X-ray nanotomography (Figure S3). Multiscale imaging revealed different sizes of the Ni-rich particles produced from molten salt corrosion by the $CeCl_3$ additive.

Compared to the Ni-20Cr corrosion in KCl-$MgCl_2$ without the additives[16,17] the major morphological difference for Ni-20Cr corroded in KCl-$MgCl_2$ with 1 wt % $CeCl_3$ was that there were no obvious pores formed in the alloy. The added $CeCl_3$ decreased the extent of corrosion of Cr in the molten KCl-$MgCl_2$. The exact cause of this can be quite complex and we briefly discuss the factors that are involved in this process. First, although Ce^{3+} is stable in molten salt, it can be oxidized to Ce^{4+}, which is then unstable in molten salt[24] and thus can be reduced back to Ce^{3+}. It is possible that oxidation of Ce^{3+} consumed the oxidants present in the molten salt, leading to less corrosion of the Cr and resulting in suppression of corrosion propagation. Additionally, the formation of the complex bicontinuous structure as observed previously is a result of a delicate balance between the Ni surface diffusion and Cr dissolution processes[16,17]; thus, any changes in either the surface diffusion rate due to the change of the salt compositions, or the Cr dissolution rate due to changes in redox potentials, can shift the kinetics of the morphological evolution. We will discuss the mechanisms behind different morphological evolution pathways
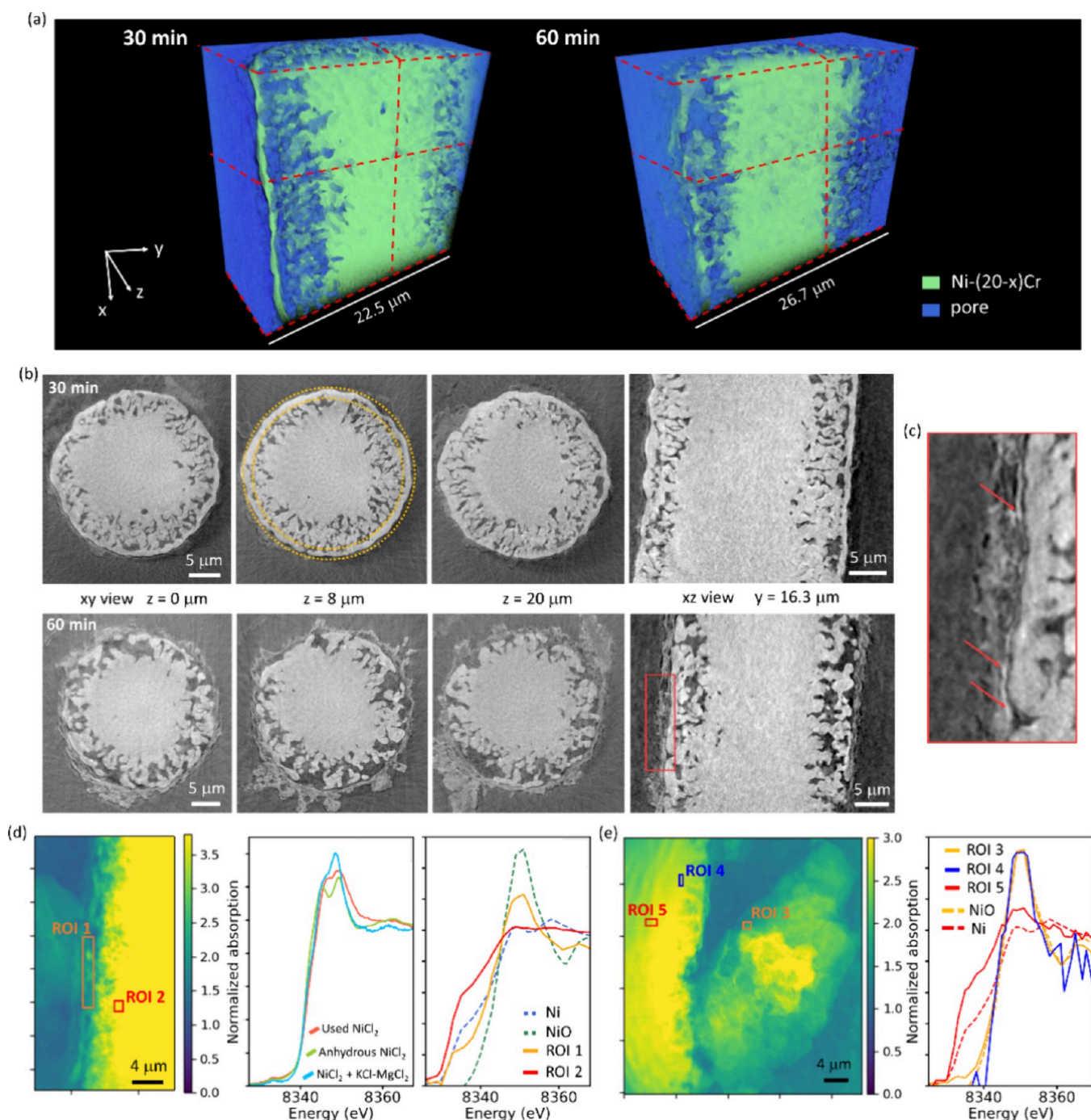
Figure 3. 3D (a) and pseudo-2D *xy* views (b) at different *z* slices, with the locations indicated by red dashed lines, and *xz* views (b) of Ni-(20-*x*)Cr after reacting with 1 wt % NiCl$_2$ in molten KCl-MgCl$_2$ (50−50 mol %) for 30 and 60 min. The yellow dashed circles highlight the surface layer observed at 30 min. The red frame highlights an expanded view in (c). (c) The expanded image of the *xz* view obtained after 60 min shows a different image contrast for the remnant salt at the surface of the sample. (d, e) 2D XANES images collected at two locations (distance ∼2000 μm along the vertical direction) with normalized Ni K-edge XANES images for different regions of interest (ROIs). The spectra from the sample ROIs are compared with reference spectra, including NiCl$_2$ used for the sample, the standard compounds Ni, NiO, anhydrous NiCl$_2$, and 1 wt % NiCl$_2$ melted with 50−50 mol % KCl-MgCl$_2$ after cooling.

at the end of this article, together with a range of different morphologies.

Ni-20Cr Corrosion in Molten KCl-MgCl$_2$ (50−50 mol %) with 1 wt % NiCl$_2$. The reaction of Ni-20Cr with 1 wt % NiCl$_2$ in molten KCl-MgCl$_2$ (50−50 mol %) at 700 °C was also investigated for 30 and 60 min (Video S2). As shown in Figure 3, compared to the pristine Ni-20Cr, pores were formed on the surface extending over several micrometers toward the center of

the sample. The corrosion was consistent along the wire, which was shown in the 2D *xy* views for different *z* locations at 0, 8, and 20 μm. When reacted for 30 min, the microwire developed a dense (nonporous) layer at the surface (between the two dashed circles in Figure 3b for *z* = 8 μm). After 60 min, the surface layer was broken (Figure 3b). The pores were larger than the pores seen at 30 min. However, the progression of pores into the center of the sample was not obvious between the two time
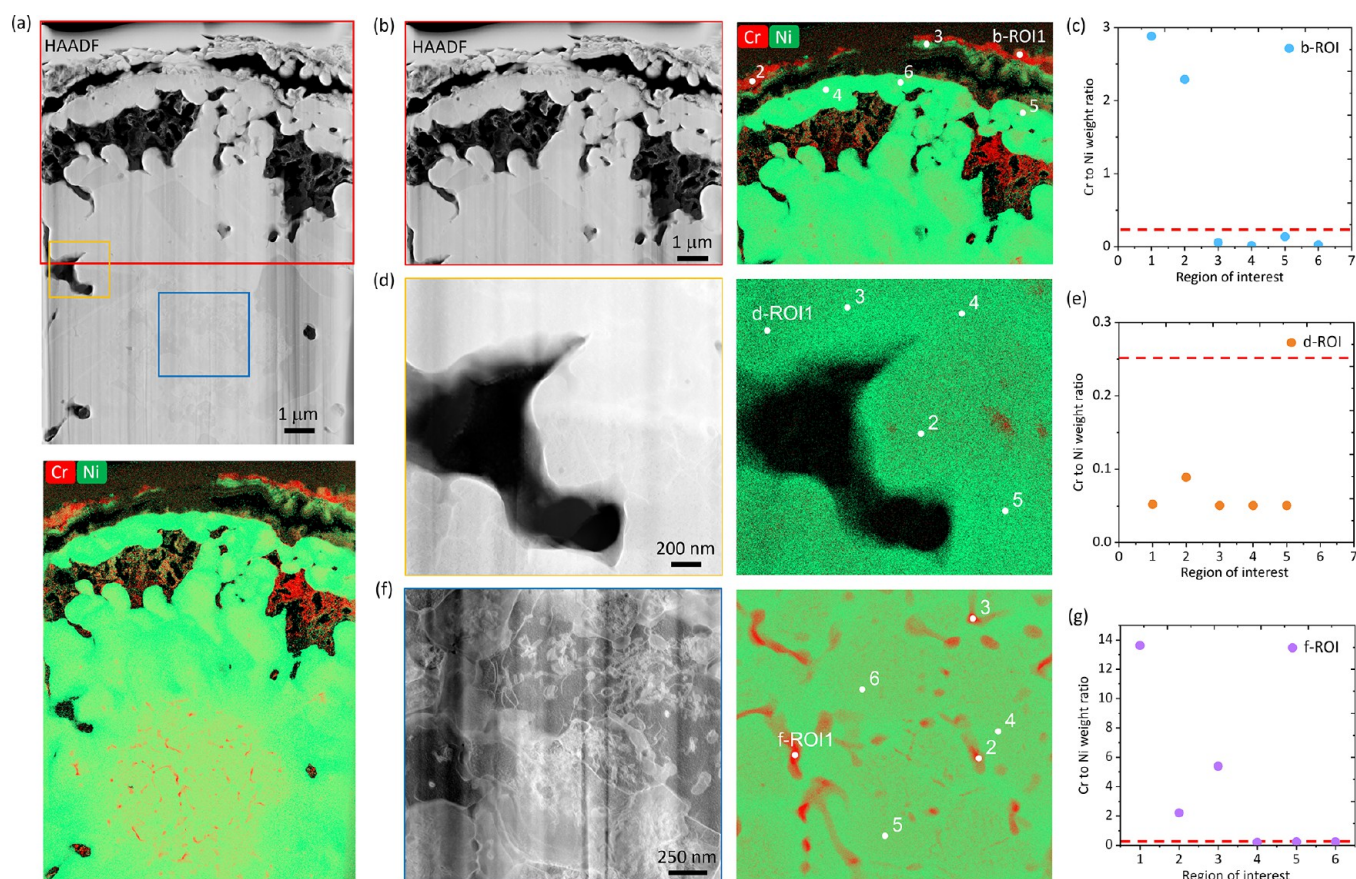
Figure 4. HAADF/STEM analysis of Ni and Cr in Ni-(20-*x*)Cr at different locations from the surface to the center after a 60 min reaction at 700 °C. (a) Overview of the corroded sample with the Cr and Ni distributions. The red, yellow, and blue frames correspond to the regions in (b), (d), and (f). (b, c) Surface region with the Cr to Ni weight ratio at different ROIs (b-ROIs). (d, e) A local pore region with the Cr to Ni weight ratios at d-ROIs. (f, g) Near center region showing Cr segregation along grain boundaries with the Cr to Ni weight ratio at f-ROIs. The red dashed line in (c, e, and g) shows the original Cr to Ni weight ratio of 0.25.

points. The remnant salt surrounding the corroded wire was identified based on its different imaging contrast. Some brighter spots (with smaller X-ray attenuations), such as those indicated by the red arrows in Figure 3c, were observed in the remnant salt, which suggests the presence of undissolved corrosion products in the salt.

2D XANES imaging was conducted at two locations for the sample reacted for 60 min (Figure 3d,e) to determine the chemical compositions near the interface between the corroded wire and remnant salt. We first exams the H_2O content in the used $NiCl_2$. The $NiCl_2$ added to the sample (Figure 3d) did not show the same double-peak postedge feature as the anhydrous $NiCl_2$ standard, indicating that the added $NiCl_2$ was not completely anhydrous. Thus, adding $NiCl_2$ likely introduced moisture into the purified KCl-$MgCl_2$. Additionally, on the effect of mixing additives into the base salt, the fused $NiCl_2$ in the KCl-$MgCl_2$ also showed different XANES features compared to the initial $NiCl_2$ added to the sample, indicating a change in structure caused by mixing the $NiCl_2$ with the KCl-$MgCl_2$ salt. The salt region near the wire (ROI 1) contained a mixture of Ni and NiO because the pre-edge feature (~8335 eV) was similar to that of Ni, but the postedge peak was similar to that of NiO. The corroded wire (ROI 2) remained as Ni. Figure 3d shows a large remnant salt region. For ROI 3 in the salt and ROI 4 in the salt at the interface, the XANES images were the same as that of NiO. For ROI 5, the uncorroded region remained as metallic Ni.

The presence of NiO in the remnant salt was the result of moisture impurity from the $NiCl_2$. The formation of NiO from $NiCl_2$ hydrolysis and the NiO passivation mechanism have been discussed in the literature for Ni corrosion with H_2O vapor in $LiCl$-KCl.[25] No insoluble $NiCl_2$ or NiO was identified in the sample (Figure S4), suggesting NiO was not introduced before the experiment. The Ni from Ni-20Cr reacted in the molten salt due to the introduction of H_2O from the $NiCl_2$ used in this experiment. Since the standard redox potential of $NiCl_2$/Ni (vs Cl_2/Cl^-) at 700 °C is more positive than those of $CrCl_2$/Cr and $CrCl_3$/Cr (vs Cl_2/Cl^-),[11,26] the Ni^{2+} ions from $NiCl_2$ and the dissolved Ni^{2+} reacted as oxidant to promote the Cr reaction, forming Ni. Then Ni could be oxidized and form NiO, as identified by XANES imaging. Overall, the presence of $NiCl_2$ and H_2O accelerated the corrosion of Ni-20Cr. An in situ X-ray nanotomography experiment was conducted to observe the morphological change of Ni-20Cr in molten KCl-$MgCl_2$ with the addition of anhydrous $NiCl_2$ (Figure S5). The corrosion is severe compared to the sample with $NiCl_2$ and moisture. The Ni 2D XANES (Figure S6) shows that only Ni presents in the corroded wire, interface and remaining salt, without the oxide formation at the surface of the sample.

Another effect of adding $NiCl_2$ is that the surface mobility of Ni could have increased. Recently, Ghaznavi et al. studied the effects of 1 and 3 wt % anhydrous $NiCl_2$ on electrochemical dealloying of the $Fe_{32}Ni_{68}$ alloy in molten $LiCl$-KCl-$MgCl_2$ at 350 °C.[27] Increasing the amount of $NiCl_2$ in the molten salt
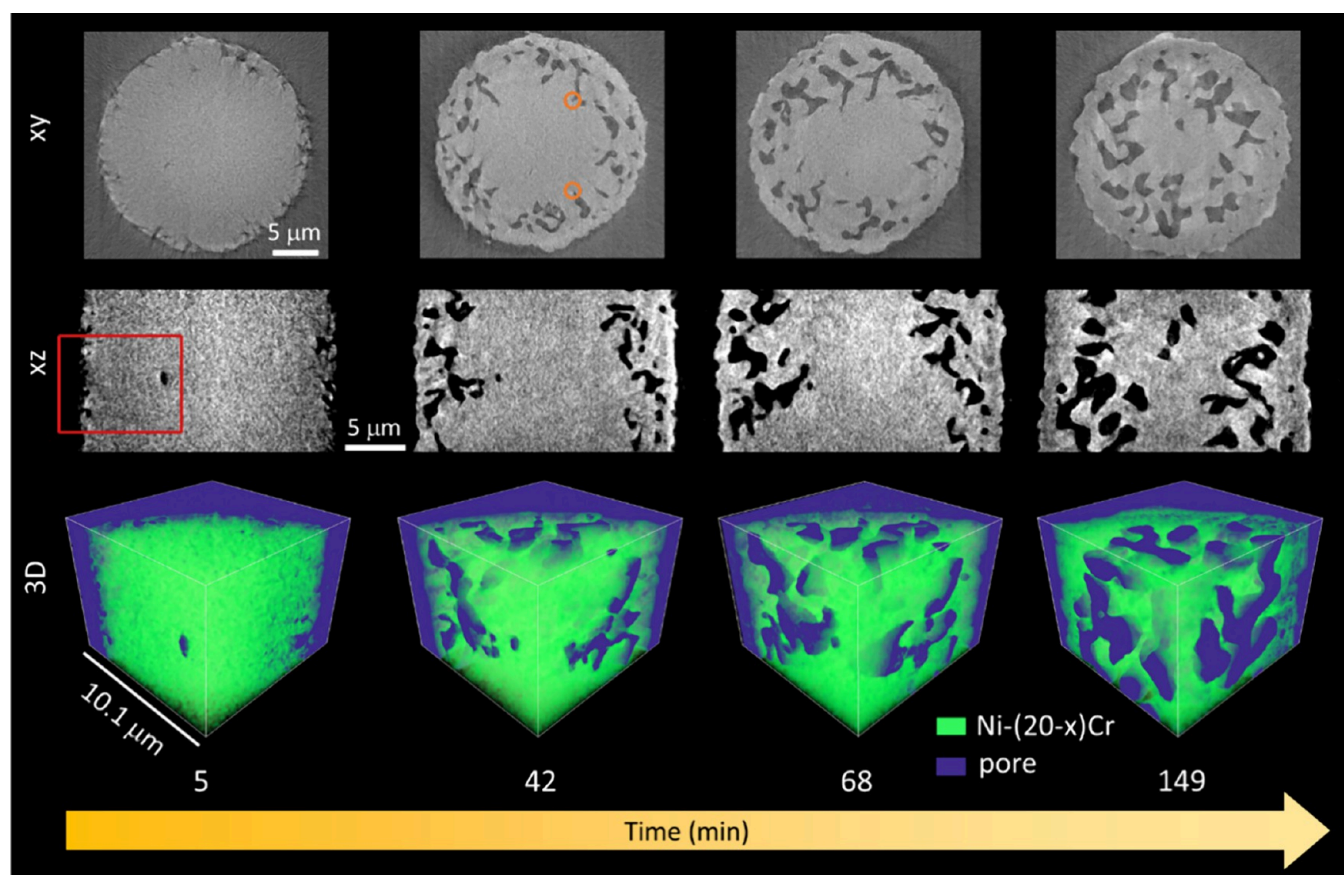
Figure 5. 2D pseudo cross-sectional views (*xy* and *xz*) and 3D volume renderings showing the morphological evolution of Ni-20Cr in molten KCl-MgCl$_2$ (50−50 mol %) with 1 wt % EuCl$_3$ as a function of reaction time. The morphological changes showed mixed behaviors: a bicontinuous porous structure formed as in percolation dealloying[16,32] with features near the reaction front similar to those from intergranular corrosion (orange circle in the *xy* view). The red frame shows the 3D visualization region.

increased the corrosion rate of Fe$_{32}$Ni$_{68}$; upon adding 3 wt % NiCl$_2$, ligaments at the original alloy/molten salt interface were broken, which was consistent with the broken surface layers observed in this work.

Figures 4a and S7 show overviews of the elemental distributions in the corroded sample. Different regions highlighted by the frames with different colors were analyzed further, denoted in Figure 4b,d,f. The surface region with remnant salt (Figure 4b) shows Cr- (b-ROI1−2) and Ni-rich (b-ROI3) regions. Figure 4c shows that b-ROI1 contains 67.2 wt % Cr and 23.3 wt % Ni and b-ROI2 has 56.0 wt % Cr and 24.5 wt % Ni, while 1.3 wt % Cr and 98.3 wt % Ni was in b-ROI3. The Cr and Ni weight ratios in the ROIs are shown in Table S2. To identify the chemical compounds presented in the Cr-rich and Ni-rich regions, correlations of Cr and Ni concentrations with respect to O and Cl concentrations were analyzed for selected areas in each region with scatter plots, as shown in Figure S8. For the Cr-rich region, the distributions of Cr and O were negatively correlated, meaning that the compound was not a Cr oxide. The correlation between Cr and Cl was less clear. Since the salt was chloride-based and Cr can dissolve in the salt, it is possible that the Cr-rich region resulted from accumulation of CrCl$_3$ (or CrCl$_2$). Future chemical characterizations such as X-ray photoelectron spectroscopy (XPS) will be useful to determine the formed Cr species. For the Ni-rich region, neither the Ni-to-O or Ni-to-Cl scatter plots showed obvious trends, but NiO was identified in the salt via XANES imaging (Figure 3d,e). The Ni-rich and Cr-rich regions observed with STEM/EDS were in the remnant salt,

which is consistent with the heterogeneous sample surface observed with X-ray nanotomography (Figure 3c).

For b-ROI4, 5, and 6 (Figure 4b) that are on the corroded alloy surface, these regions were Ni-rich and contained less Cr than pristine Ni-20Cr, suggesting preferable dissolution of Cr. Furthermore, the Cr and Ni weight ratio change was analyzed for a region near a pore within the sample (Figure 4d,e). A significantly lower Cr-to-Ni weight ratio compared to Ni-20Cr shows the formation of the Ni-rich layer at the alloy/molten salt interface.

Finally, Figure 4f,g shows a center region that was not close to the corroded region. Cr segregation was observed at the grain boundary (f-ROI1−3), while Ni-20Cr was preserved in the grains (f-ROI4−6). Previous studies have shown depletion of Cr along the grain boundaries in corroded regions[28]; additionally, this study shows enrichment of Cr at the grain boundary in the uncorroded region. The Cr concentration gradient from the uncorroded Ni-20Cr center region to the alloy/molten salt interface provides a driving force for outward Cr diffusion. The diffusion coefficient for Cr along the grain boundary is $\sim 10^4$ times higher than the bulk diffusion coefficient of Cr in Ni-based alloys[29]; thus, Cr is more likely to diffuse along the grain boundaries. Thus, this work indicates that for the regions in alloys away from the corrosion reaction front, the high temperature environment and the concentration gradient of the corroding elements drive elemental segregation along the grain boundaries, which affects long-term corrosion and the mechanical properties of the structural alloys.
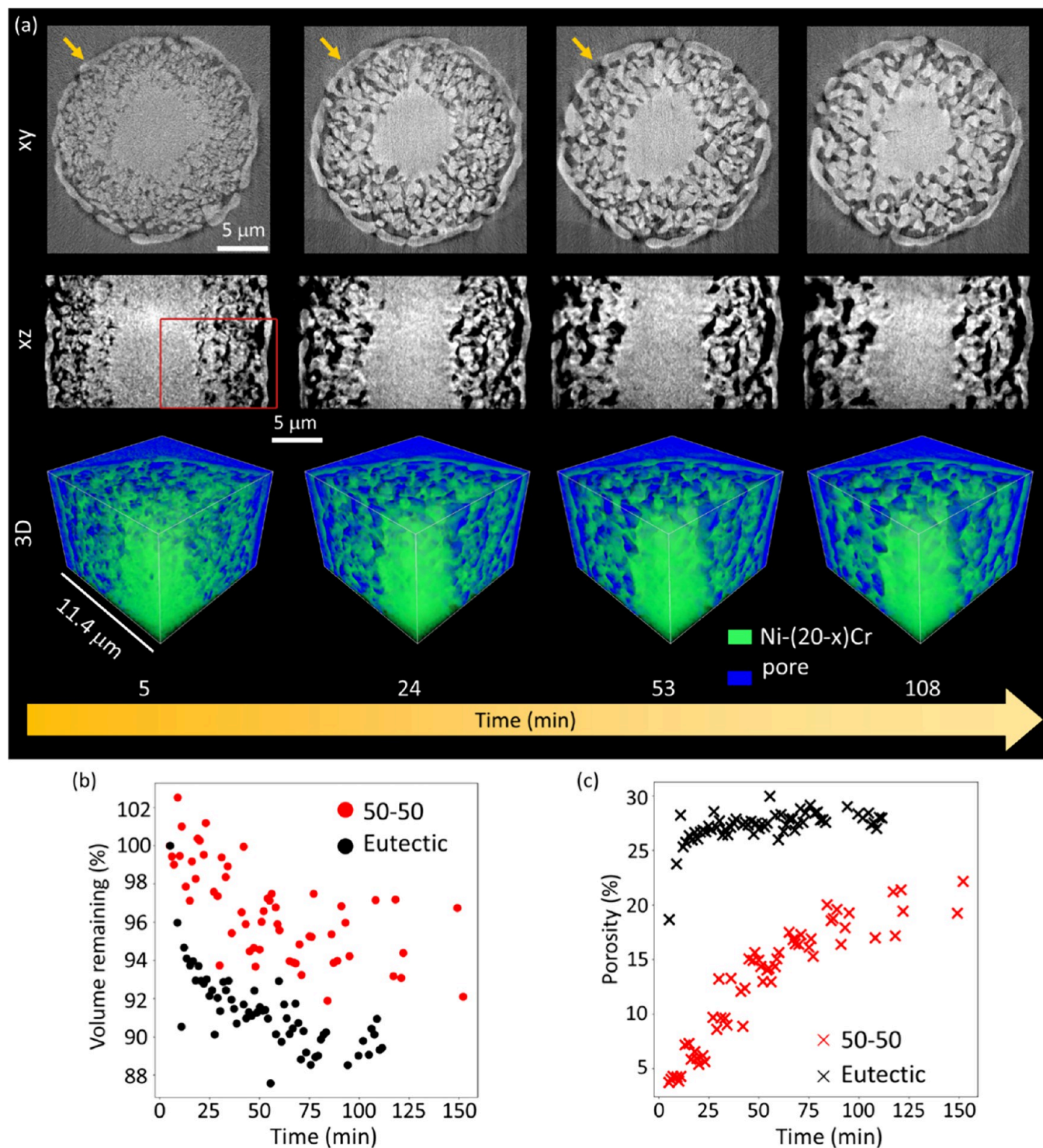
Figure 6. Morphological evolution of Ni-20Cr in molten eutectic KCl-MgCl$_2$ (68−32 mol %) with 1 wt % EuCl$_3$ as a function of reaction time. (a) 2D pseudo cross-sectional views (*xy* and *xz*) and 3D volume rendering. The red frame indicates the 3D visualization region. (b, c) Remaining volume and porosity changes of Ni-20Cr in 50−50 and eutectic KCl-MgCl$_2$ with 1 wt % EuCl$_3$ as a function of reaction time.

In Situ Study of Ni-20Cr Corrosion by 1 wt % EuCl$_3$ in KCl-MgCl$_2$ at Eutectic and Off-Eutectic Composition. The in situ corrosion of Ni-20Cr in 50−50 mol % and eutectic (68−32 mol %) KCl-MgCl$_2$ with 1 wt % EuCl$_3$ was studied at 700 °C with synchrotron X-ray nanotomography. The ratio of salt mixture, ranging from eutectic to off-eutectic compositions, has been reported to influence the acidity−basicity of the salt[30] and can also impact corrosion behaviors. Since EuCl$_3$ has been

shown to increase the corrosion rate, there is particular interest in investigating the morphological evolution differences in salt compositions with EuCl$_3$ additives. First, Figures 5 and 6 show the 2D and 3D morphological evolution processes occurring in Ni-20Cr after different reaction times in 50−50 mol % and eutectic KCl-MgCl$_2$ with 1 wt % EuCl$_3$, respectively. Both samples showed corrosion propagation from the surface, and pores were formed in the reacted regions. Eu is a fission product,
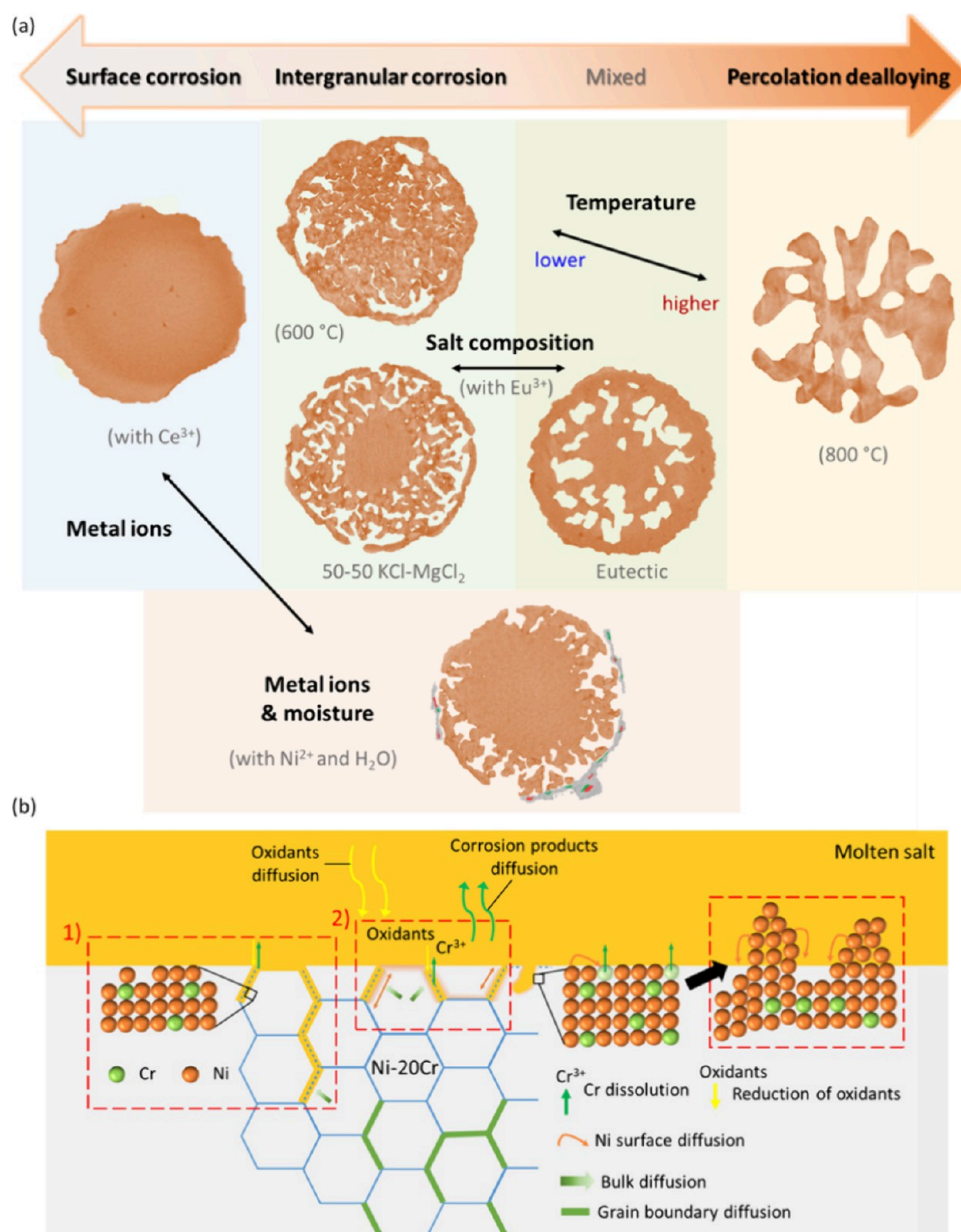
Figure 7. (a) The morphology of corroded Ni-20Cr in molten salt with different additives, reaction temperatures and salt compositions. (b) Reaction and diffusion processes affect the chemical and morphological changes occurring at the interfaces of alloys in molten salt.

and strong oxidants can be reduced in molten salt, thereby increasing the overall corrosion driving force and promoting the oxidation of Cr.[31] However, the extent of morphological evolution differed significantly for the two different salt concentrations of KCl-MgCl$_2$.

For 50−50 KCl-MgCl$_2$, salt exposure led to formation of a bicontinuous porous structure with features indicating intergranular corrosion at the reaction front. While pore showed at the surface within 5 min, a surface layer was formed with longer reaction times. For eutectic KCl-MgCl$_2$, clear intergranular corrosion was observed. For the same reaction time of 5 min, faster corrosion was observed in the eutectic salt compared to the 50−50 KCl-MgCl$_2$ mixture, as indicated by the corrosion depth. Breakage of the surface layer (the yellow arrows point to the same location) was observed with the increase in reaction time. The remaining volume and porosity as a function of reaction time are compared for the two salt ratios in Figure 6b,c,

respectively. The sample in the KCl-MgCl$_2$ eutectic underwent more significant corrosion than the sample in 50−50 KCl-MgCl$_2$ with EuCl$_3$, as indicated by the lower alloy volume remaining (∼90% compared to 94%) and the higher porosity (∼27% compared to 22%). In addition, the more rapid changes in both the volume and the porosity, especially during the early times, for the sample in eutectic KCl-MgCl$_2$ than for the 50−50 KCl-MgCl$_2$ also indicates the faster reaction kinetics in the former case.

Diffusion and Reaction Mechanisms Affecting Morphological Evolution of Ni-20Cr in a Molten Chloride Salt Mixture. In this and our prior work, series of experiments were conducted to study the morphological evolutions of Ni-20Cr in molten KCl-MgCl$_2$ at different reaction temperatures,[16,17] different salt compositions (50−50 and 68−32 mol % of KCl-MgCl$_2$), and metal ions resembling the corrosion products from common structural materials or fission products (Ni^{2+}, Ce^{3+}, and

Eu^{3+}) in molten salt applications using the same sample preparation and experimental setup. A morphological library based on molten salt corrosion as a function of reaction conditions is provided in Figure 7a. The figure summarizes a morphological transition from surface corrosion to intergranular corrosion to percolation dealloying forming a bicontinuous structure of metal-pore interconnected networks with the change of metal ions, temperature and salt compositions. The addition of metal ions (and moisture) introduces different corrosion phenomena, including surface corrosion (with Ce^{3+}) and severe corrosion with accumulation of Ni^{2+} and Cr^{2+}/Cr^{3+} in the remnant salt. With increasing temperature (from 500 to 800 °C) and change of salt composition (from 50 to 50 molar ratio to eutectic salts with added Eu^{3+}), the morphological evolution pathway changes from intergranular corrosion to predominantly percolation dealloying. Note that mixed features of the bicontinuous structure with a shorter dealloying front indicating intergranular corrosion can also be present, as shown in the case with the eutectic salt. Molten salt corrosion is a result of fundamental physical and chemical processes, namely, different chemical reactions and mass transport mechanisms, including diffusion at surfaces/interfaces and in bulk (solid and liquid) materials. Therefore, changes in the engineering conditions alter the underlying changes in diffusion and reaction processes that occur during molten salt corrosion. Below, the mechanistic understanding gained through our investigations is summarized.

In electrochemical dealloying, various morphologies are formed below and above the critical potential, determined by the balance between surface dissolution and diffusion with a percolation pathway.[33] Reactions of Ni-20Cr in molten salt are similar to electrochemical dealloying of binary alloys but are more complicated. The major morphological evolutions from intergranular to percolation pores were affected by (1) grain boundaries as shortcuts for reactions or diffusion[34]; (2) the relative rates for the chemical reaction of Cr dissolution into Cr^{2+}/Cr^{3+} ions, and surface diffusion of Ni atoms, as shown in Figure 7b. For intergranular corrosion, in Figure 7b-1, Ni surface diffusion is much faster than Cr dissolution at the grain surface. Because Cr dissolution occurs at the grain boundaries, first consuming the oxidants in the salt and creating a tortuous path, the rate of Cr dissolution at the grain surface decreases. Low temperature and reactants with more negative redox potentials than Cr also decreased the Cr dissolution. When surface Cr atoms react, fast surface diffusion of Ni quickly covers the surface without exposing more Cr atoms. Thus, after corrosion, a Ni-rich grain surface forms. In another case (Figure 7b-2), if the rates of the Cr dissolution and Ni surface diffusion are comparable, these two processes work together via the percolation dealloying mechanism. According to the percolation dealloying process proposed for aqueous solution, when the concentration of a reactive component exceeds a critical threshold (percolation limit), continuous atomic-scale pathways of that component form, and thus eliminate the need for solid-state transport to facilitate selective dissolution. In the case of a nearly random solid solution alloy, these pathways are evenly distributed in all directions, leading to the development of isotropic bicontinuous dealloyed structures.[35] Additionally, corrosion can still occur along the grain boundary, as with dealloying of binary alloys in liquid metals[36] at high temperature. An alternative hypothesis offered here, which will be examined in the future, is that corrosion primarily occurs through some types of the grain boundaries, followed by rapid surface diffusion

and coarsening that leads to surface smoothing at the metal-salt interface and thus to a structure that resembles those formed via percolation dealloying.

On the other hand, the addition of metal ions affects the rate of Cr reaction. The addition of ions decelerates the Cr reaction (Ce^{3+}) and surface corrosion occurs, leaving a Ni-rich surface. Research has shown that excess Mg[37] or Li[38] metal can be added to provide a reactive metal to enable this type of redox control. In the opposite scenario, the addition of metal ions increases the oxidation ability of the molten salt, accelerating Cr oxidation (Eu^{3+} and Ni^{2+}) or causing both Ni and Cr oxidation (due to moisture or oxygen impurities). In these cases, large pores form and the interface of the corroded region is Ni-rich. In the salt near the interface, the accumulation of Ni or Cr ions may happen due to fast reaction. Lastly, the loss of Cr at the interface causes a concentration gradient of Cr from the intact region to the corroded region, providing the driving force for the diffusion of Cr along the grain boundary (green highlights in Figure 7b).

■ CONCLUSIONS

This work summarizes the morphological changes occurring during Ni-20Cr alloy corrosion in molten $KCl-MgCl_2$ with various temperatures, salt compositions and metal ions resulting from fission and reactions of structural materials. Planar reactions at the surface, intergranular corrosion, and percolation dealloying forming bicontinuous structures were observed under varying conditions. We hypothesize that the competition between the reaction of a less noble element (e.g., Cr) and surface diffusion of a more noble element (e.g., Ni) changes under different conditions and thus results in different corrosion morphologies. Future studies are needed to either experimentally characterize or construct simulation models that consider reaction and diffusion rates. This will provide a direct comparison of molten salt corrosion under various conditions, leading to different morphological evolutions. Furthermore, the diffusion processes, chemical activity and physical or chemical properties of the salt and alloy that influence the molten salt corrosion mechanism were illustrated. This work provides a step in linking the application parameters of molten salt reactors to the corrosion morphologies of the materials through the understanding of the underlying mechanisms. Additionally, this work further demonstrates the use of synchrotron X-ray nanotomography and spectroscopic imaging, coupled with STEM analysis, to study materials in molten salt environments. The molten salt research community can continue to benefit from these advanced characterization techniques to understand the transition of materials under evolving conditions, as has also been demonstrated in other energy application research communities.[39] Beyond this work, future studies can provide further quantitative analyses and theoretical understanding of these complex interacting mechanisms.

■ ASSOCIATED CONTENT

Data Availability Statement

The digital data for all figures, tables, charts, and any other media contained in this publication and its associated Supporting Information files will be made accessible on the Zenodo repository under Digital Object Identifier (DOI): 10.5281/zenodo.10408543.

ⓢ Supporting Information

The Supporting Information is available free of charge at https://pubs.acs.org/doi/10.1021/acsami.4c02049.

Segmentation and quantification of the in situ data sets (Ni-20Cr in eutectic and 50−50 mol % KCl-MgCl$_2$ with 1 wt %) EuCl$_3$; selected regions for analyzing the atomic ratio of Ni and Cr in the Ni-(20-x)Cr after reacting with 1 wt % CeCl$_3$ in KCl-MgCL$_2$; Cr L$_3$/L$_2$ integrated intensity ratio from EELS spectra; particle size determination; homogeneous salt before experiment; elemental distribution of salt elements after corrosion; morphological evolution of Ni-20Cr in KCl-MgCl$_2$ with anhydrous NiCl$_2$; Ni 2D XANES; Cr and Ni weight ratios from STEM/EDS for the ROIs in Figure 4; corrections of Cr to Cl, Cr to O, Ni to Cl and Ni to O (PDF)

3D view of the corroded Ni-20Cr in the salt with CeCl$_3$ for 30 min (MPG)

3D view of the corroded Ni-20Cr in the salt with NiCl$_2$ for 30 and 60 min (MPG)

■ AUTHOR INFORMATION

Corresponding Author

Yu-chen Karen Chen-Wiegart − *Materials Science and Chemical Engineering, Stony Brook University, Stony Brook, New York 11794, United States; National Synchrotron Light Source II (NSLS-II), Brookhaven National Laboratory, Upton, New York 11973, United States;* ● orcid.org/0000-0003-4445-2159; Email: Karen.Chen-Wiegart@stonybrook.edu

Authors

Xiaoyang Liu − *Materials Science and Chemical Engineering, Stony Brook University, Stony Brook, New York 11794, United States;* ● orcid.org/0000-0002-9326-2135

Kaustubh K. Bawane − *Advanced Characterization Department, Idaho National Laboratory, Idaho Falls, Idaho 83404, United States*

Charles Clark − *Materials Science and Chemical Engineering, Stony Brook University, Stony Brook, New York 11794, United States;* ● orcid.org/0000-0001-6642-8489

Yuxiang Peng − *Materials Science and Chemical Engineering, Stony Brook University, Stony Brook, New York 11794, United States*

Michael E. Woods − *Advanced Technology of Molten Salts Department, Idaho National Laboratory, Idaho Falls, Idaho 83415, United States;* ● orcid.org/0000-0001-8685-6026

Phillip Halstenberg − *Department of Chemistry, University of Tennessee, Knoxville, Tennessee 37996, United States; Chemical Sciences Division, Oak Ridge National Laboratory, Oak Ridge, Tennessee 37831, United States;* ● orcid.org/0000-0002-6030-4503

Xianghui Xiao − *National Synchrotron Light Source II (NSLS-II), Brookhaven National Laboratory, Upton, New York 11973, United States*

Wah-Keat Lee − *National Synchrotron Light Source II (NSLS-II), Brookhaven National Laboratory, Upton, New York 11973, United States*

Lu Ma − *National Synchrotron Light Source II (NSLS-II), Brookhaven National Laboratory, Upton, New York 11973, United States*

Steven Ehrlich − *National Synchrotron Light Source II (NSLS-II), Brookhaven National Laboratory, Upton, New York 11973, United States*

Sheng Dai − *Chemical Sciences Division, Oak Ridge National Laboratory, Oak Ridge, Tennessee 37831, United States;* ● orcid.org/0000-0002-8046-3931

Katsuyo Thornton − *Department of Materials Science and Engineering, University of Michigan, Ann Arbor, Michigan 48109, United States;* ● orcid.org/0000-0002-1227-5293

Mingyuan Ge − *National Synchrotron Light Source II (NSLS-II), Brookhaven National Laboratory, Upton, New York 11973, United States;* ● orcid.org/0000-0001-5682-7443

Ruchi Gakhar − *Advanced Technology of Molten Salts Department, Idaho National Laboratory, Idaho Falls, Idaho 83415, United States;* ● orcid.org/0000-0002-2829-3533

Lingfeng He − *Advanced Characterization Department, Idaho National Laboratory, Idaho Falls, Idaho 83404, United States; Department of Nuclear Engineering, North Carolina State University, Raleigh, North Carolina 27695, United States*

Author Contributions

Y.-c.K.C.-W. and X.L. developed the research idea with input from K.K.B., M.E.W., R.G., and L.H.; X.L. conducted the synchrotron experiments and data analyses under the supervision of Y.-c.K.C.-W and with support from M.G., X.X., and W.-K.L. for FXI, as well as from L.M. and S.E. for QAS; C.C. conducted the data analysis and visualization for the in situ study under the guidance of X.L.; K.K.B. and L.H. conducted the TEM characterization. M.E.W. and P.H. prepared the salts under the supervision of R.G. and S.D., respectively. K.T. contributed to data interpretation and the discussion of mechanisms. X.L. and Y.-c.K.C.-W. wrote the manuscript with contributions from all coauthors.

Notes

The authors declare no competing financial interest.

■ ACKNOWLEDGMENTS

■ REFERENCES

(1) (a) McMurray, J.; Johnson, K.; Agca, C.; Betzler, B.; Kropaczek, D.; Besmann, T.; Andersson, D.; Ezell, N. *Roadmap for thermal property measurements of Molten Salt Reactor systems*; 2021. (b) Serp, J.; Allibert,

M.; Benes, O.; Delpech, S.; Feynberg, O.; Ghetta, V.; Heuer, D.; Holcomb, D.; Ignatiev, V.; Kloosterman, J. L.; et al. The molten salt reactor (MSR) in generation IV: Overview and Perspectives. *Prog. Nucl. Energy* **2014**, *77*, 308−319.

(2) (a) Dine, W. J.; Bonk, A.; Bauer, T. Molten Chloride Salts for Next Generation CSP Plants: Selection of Promising Chloride Salts & Study on Corrosion of Alloys in Molten Chloride Salts. In *24th International Conference on Concentrating Solar Power and Chemical Energy Systems (SolarPACES)*; Casablanca, Morocco, 2019; vol *2126*. (b) Bell, S.; Steinberg, T.; Will, G. Corrosion mechanisms in molten salt thermal energy storage for concentrating solar power. *Renewable Sustainable Energy Rev.* **2019**, *114*, No. 109328.

(3) (a) Wang, D.; Yang, J. G.; He, P.; Zhou, H. S. A low-charge-overpotential lithium-CO2 cell based on a binary molten salt electrolyte. *Energy Environ. Sci.* **2021**, *14* (7), 4107−4114. (b) Pang, Q.; Meng, J.; Gupta, S.; Hong, X.; Kwok, C. Y.; Zhao, J.; Jin, Y.; Like, Xu; Karahan, O.; Wang, Z.; Toll, S.; Mai, L.; Nazar, L. F.; Balasubramanian, M.; Narayanan, B.; Donald, R. Sadoway Fast-charging aluminium−chalcogen batteries resistant to dendritic shorting. *Nature* **2022**, *608*, 704−711.

(4) Raiman, S. S.; Lee, S. Aggregation and data analysis of corrosion studies in molten chloride and fluoride salts. *J. Nucl. Mater.* **2018**, *511*, 523−535.

(5) Pillai, R.; Raiman, S. S.; Pint, B. A. First steps toward predicting corrosion behavior of structural materials in molten salts. *J. Nucl. Mater.* **2021**, *546*, No. 152755.

(6) Zhu, M.; Zeng, S.; Zhang, H. H.; Li, J. Y.; Cao, B. Y. Electrochemical study on the corrosion behaviors of 316 SS in HITEC molten salt at different temperatures. *Sol. Energy Mater. Sol. Cells* **2018**, *186*, 200−207.

(7) Zhu, Z. B.; Huang, H. F.; Lei, G. H.; Wu, Y. P.; Ren, C. L.; Liu, A. W.; Zhu, Z. Y. Synergistic effect of irradiation and molten salt corrosion: Acceleration or deceleration? *Corros. Sci.* **2021**, *185*, No. 109434.

(8) (a) Ding, W. J.; Gomez-Vidal, J.; Bonk, A.; Bauer, T. Molten chloride salts for next generation CSP plants: Electrolytical salt purification for reducing corrosive impurity level. *Sol. Energy Mater. Sol. Cells* **2019**, *199*, 8−15. (b) Ong, T. C.; Sarvghad, M.; Lippiatt, K.; Griggs, L.; Ryan, H.; Will, G.; Steinberg, T. A. Review of the solubility, monitoring, and purification of impurities in molten salts for energy storage in concentrated solar power plants. *Renewable & Sustainable Energy Reviews* **2020**, *131*, No. 110006.

(9) Pavlik, V.; Kontrik, M.; Boca, M. Corrosion behavior of Incoloy 800H/HT in the fluoride molten salt FLiNaK + MFx (MFx = CrF3, FeF2, FeF3 and NiF2). *New J. Chem.* **2015**, *39* (12), 9841−9847.

(10) Zhang, J. S. Impurities in Primary Coolant Salt of FHRs: Chemistry, Impact, and Removal Methods. *Energy Technology* **2019**, *7* (10), No. 1900016.

(11) Guo, S. Q.; Zhang, J. S.; Wu, W.; Zhou, W. T. Corrosion in the molten fluoride and chloride salts and materials development for nuclear applications. *Prog. Mater. Sci.* **2018**, *97*, 448−487.

(12) (a) Roy, S.; Sharma, S.; Karunaratne, W. V.; Wu, F.; Gakhar, R.; Maltsev, D. S.; Halstenberg, P.; Abeykoon, M.; Gill, S. K.; Zhang, Y. P.; et al. X-ray scattering reveals ion clustering of dilute chromium species in molten chloride medium. *Chemical Science* **2021**, *12* (23), 8026−8035. (b) Li, Q. J.; Sprouster, D.; Zheng, G. Q.; Neuefeind, J. C.; Braatz, A. D.; McFarlane, J.; Olds, D.; Lam, S.; Li, J.; Khaykovich, B. Complex Structure of Molten NaCl-CrCl3 Salt: Cr-Cl Octahedral Network and Intermediate-Range Order. *Acs Applied Energy Materials* **2021**, *4* (4), 3044−3056.

(13) Yang, Q. F.; Ge, J. B.; Zhang, J. S. Electrochemical Study on the Kinetic Properties of Fe2+/Fe, Ni2+/Ni, Cr2+/Cr and Cr3+/Cr2+ in Molten MgCl2-KCl-NaCl Salts. *J. Electrochem. Soc.* **2021**, *168* (1), No. 012504, DOI: 10.1149/1945-7111/abdafc.

(14) (a) Knosalla, C.; Lau, M.; Schmies, L.; Lippmann, W.; Hurtado, A. Investigation on the Corrosion Behavior of Nickel-Base Alloys in Molten Chlorides for Sensible Heat Energy Applications. *Adv. Eng. Mater.* **2020**, *22* (7), No. 2000099. (b) Liu, Y. Y.; Song, Y. L.; Ai, H.; Shen, M.; Liu, H. T.; Zhao, S. F.; Liu, Y. C.; Fei, Z. J.; Fu, X. B.; Cheng, J.

(15) (a) Wu, F.; Roy, S.; Ivanov, A. S.; Gill, S. K.; Topsakal, M.; Dooryhee, E.; Abeykoon, M.; Kwon, G.; Gallington, L. C.; Halstenberg, P.; et al. Elucidating Ionic Correlations Beyond Simple Charge Alternation in Molten MgCl2-KCl Mixtures. *J. Phys. Chem. Lett.* **2019**, *10* (24), 7603−7610. (b) Dolzhnikov, D. D.; Dai, S. *M4FT:18OR110102182-Develop a new composite molten salt fluid exhibiting an increased heat capacity of 10%*; 2018.

(16) Liu, X. Y.; Ronne, A.; Yu, L. C.; Liu, Y.; Ge, M. Y.; Lin, C. H.; Layne, B.; Halstenberg, P.; Maltsev, D. S.; Ivanov, A. S.; et al. Formation of three-dimensional bicontinuous structures via molten salt dealloying studied in real-time by in situ synchrotron X-ray nano-tomography. *Nat. Commun.* **2021**, *12* (1), 3441.

(17) Bawane, K.; Liu, X. Y.; Gakhar, R.; Woods, M.; Ge, M. Y.; Xiao, X. H.; Lee, W. K.; Halstenberg, P.; Dai, S.; Mahurin, S.; et al. Visualizing time-dependent microstructural and chemical evolution during molten salt corrosion of Ni-20Cr model alloy using correlative quasi in situ TEM and in situ synchrotron X-ray nano-tomography. *Corros. Sci.* **2022**, *195*, No. 109962.

(18) Ge, M. Y.; Coburn, D. S.; Nazaretski, E.; Xu, W. H.; Gofron, K.; Xu, H. J.; Yin, Z. J.; Lee, W. K. One-minute nano-tomography using hard X-ray full-field transmission microscope. *Appl. Phys. Lett.* **2018**, *113* (8), No. 083109.

(19) Antonelli, S.; Ronne, A.; Han, I.; Ge, M. Y.; Layne, B.; Shahani, A. J.; Iwamatsu, K.; Wishart, J. F.; Hulbert, S. L.; Lee, W. K.; et al. Versatile compact heater design for in situ nano-tomography by transmission X-ray microscopy. *J. Synchrotron Radiat.* **2020**, *27*, 746−752.

(20) Gursoy, D.; De Carlo, F.; Xiao, X. H.; Jacobsen, C. TomoPy: a framework for the analysis of synchrotron tomographic data. *J. Synchrotron Radiat.* **2014**, *21*, 1188−1193.

(21) Ge, M. Y.; Lee, W. K. PyXAS - an open-source package for 2D X-ray near-edge spectroscopy analysis. *J. Synchrotron Radiat.* **2020**, *27*, 567−575.

(22) Ravel, B.; Newville, M. ATHENA, ARTEMIS, HEPHAESTUS: data analysis for X-ray absorption spectroscopy using IFEFFIT. *J. Synchrotron Radiat.* **2005**, *12*, 537−541.

(23) Bawane, K.; Manganaris, P.; Wang, Y. C.; Sure, J.; Ronne, A.; Halstenberg, P.; Dai, S.; Gill, S. K.; Sasaki, K.; Chen-Wiegart, Y. C. K.; et al. Determining oxidation states of transition metals in molten salt corrosion using electron energy loss spectroscopy. *Scr. Mater.* **2021**, *197*, No. 113790.

(24) Zhu, H. *Rare Earth Metal Production by Molten Salt Electrolysis*; Gerhard Kreysa, K.-I. O.; Savinell, R. F., Eds.; Springer: New York, NY, 2014.

(25) Horvath, D.; Simpson, M. F. Electrochemical Monitoring of Ni Corrosion Induced by Water in Eutectic LiCl-KCl. *J. Electrochem. Soc.* **2018**, *165* (5), C226−C233.

(26) Zhang, J. S. Electrochemistry of actinides and fission products in molten salts-Data review. *J. Nucl. Mater.* **2014**, *447* (1−3), 271−284.

(27) Ghaznavi, T.; Persaud, S. Y.; Newman, R. C. Electrochemical Corrosion Studies in Molten Chloride Salts. *J. Electrochem. Soc.* **2022**, *169* (6), No. 061502.

(28) (a) Zheng, G. Q.; Sridharan, K. Corrosion of Structural Alloys in High-Temperature Molten Fluoride Salts for Applications in Molten Salt Reactors. *Jom* **2018**, *70* (8), 1535−1541. (b) Danon, A. E.; Muransky, O.; Karatchevtseva, I.; Zhang, Z.; Li, Z. J.; Scales, N.; Kruzic, J. J.; Edwards, L. Molten salt corrosion (FLiNaK) of a Ni-Mo-Cr alloy and its welds for application in energy-generation and energy-storage systems. *Corros. Sci.* **2020**, *164*, No. 108306.

(29) Sun, H.; Zhang, P.; Wang, J. Q. Effects of alloying elements on the corrosion behavior of Ni-based alloys in molten NaCl-KCl-MgCl(2)-salt at different temperatures. *Corros. Sci.* **2018**, *143*, 187−199.

(30) Roy, S.; Liu, Y.; Topsakal, M.; Dias, E.; Gakhar, R.; Phillips, W. C.; Wishart, J. F.; Leshchev, D.; Halstenberg, P.; Dai, S.; et al. A Holistic Approach for Elucidating Local Structure, Dynamics, and Speciation in Molten Salts with High Structural Disorder. *J. Am. Chem. Soc.* **2021**, *143* (37), 15298−15308.

H. Corrosion of Cr in molten salts with different fluoroacidity in the presence of CrF3. *Corros. Sci.* **2020**, *169*, No. 108636.

(31) (a) Guo, S. Q.; Zhuo, W. Q.; Wang, Y. F.; Zhang, J. S. Europium induced alloy corrosion and cracking in molten chloride media for nuclear applications. *Corros. Sci.* **2020**, *163*, No. 108279. (b) Wang, Y. F.; Goh, B.; Nelaturu, P.; Duong, T.; Hassan, N.; David, R.; Moorehead, M.; Chaudhuri, S.; Creuziger, A.; Hattrick-Simpers, J. Integrated High-Throughput and Machine Learning Methods to Accelerate Discovery of Molten Salt Corrosion-Resistant Alloys. *Adv. Sci.* **2022**, *9* (20), No. e2200370.

(32) Ronne, A.; He, L. F.; Dolzhnikov, D.; Xie, Y.; Ge, M. Y.; Halstenberg, P.; Wang, Y. C.; Manard, B. T.; Xiao, X. H.; Lee, W. K.; et al. Revealing 3D Morphological and Chemical Evolution Mechanisms of Metals in Molten Salt by Multimodal Microscopy. *ACS Appl. Mater. Interfaces* **2020**, *12* (15), 17321−17333.

(33) (a) Sieradzki, K. CURVATURE EFFECTS IN ALLOY DISSOLUTION. *J. Electrochem. Soc.* **1993**, *140* (10), 2868−2872. (b) Wagner, K.; Brankovic, S. R.; Dimitrov, N.; Sieradzki, K. Dealloying below the critical potential. *J. Electrochem. Soc.* **1997**, *144* (10), 3545−3555. (c) Chuang, A.; Erlebacher, J. Challenges and Opportunities for Integrating Dealloying Methods into Additive Manufacturing. *Materials* **2020**, *13* (17), 3706.

(34) Badwe, N.; Chen, X.; Schreiber, D. K.; Olszta, M. J.; Overman, N. R.; Karasz, E. K.; Tse, A. Y.; Bruemmer, S. M.; Sieradzki, K. Decoupling the role of stress and corrosion in the intergranular cracking of noble-metal alloys. *Nat. Mater.* **2018**, *17* (10), 887−893.

(35) Chen, Q.; Sieradzki, K. Mechanisms and Morphology Evolution in Dealloying. *J. Electrochem. Soc.* **2013**, *160* (6), C226−C231.

(36) (a) McCue, I.; Gaskey, B.; Geslin, P. A.; Karma, A.; Erlebacher, J. Kinetics and morphological evolution of liquid metal dealloying. *Acta Mater.* **2016**, *115*, 10−23. (b) Joo, S.-H.; Jeong, Y. B.; Wada, T.; Okulov, I. V.; Kato, H. Inhomogeneous dealloying kinetics along grain boundaries during liquid metal dealloying. *J. Mater. Sci. Technol.* **2022**, *106*, 41−48. DOI: 10.1016/j.jmst.2021.07.023.

(37) Hanson, K.; Sankar, K. M.; Weck, P. F.; Startt, J. K.; Dingreville, R.; Deo, C. S.; Sugar, J. D.; Singh, P. M. Effect of excess Mg to control corrosion in molten MgCl2 and KCl eutectic salt mixture. *Corros. Sci.* **2022**, *194*, No. 109914.

(38) Sankar, K. M.; Singh, P. M. Effect of Li metal addition on corrosion control of Hastelloy N and stainless steel 316H in molten LiF-NaF-KF. *J. Nucl. Mater.* **2021**, *555*, No. 153098.

(39) (a) Chen, J. N.; Yang, Y.; Tang, Y. S.; Wang, Y. F.; Li, H.; Xiao, X. H.; Wang, S. N.; Darma, M. S. D.; Etter, M.; Missyul, A.; et al. Constructing a Thin Disordered Self-Protective Layer on the LiNiO2 Primary Particles Against Oxygen Release. *Adv. Funct. Mater.* **2023**, *33* (6), No. 2211515. (b) Hua, W. B.; Wang, S. N.; Knapp, M.; Leake, S. J.; Senyshyn, A.; Richter, C.; Yavuz, M.; Binder, J. R.; Grey, C. P.; Ehrenberg, H.; et al. Structural insights into the formation and voltage degradation of lithium- and manganese-rich layered oxides. *Nat. Commun.* **2019**, *10*, 5365.